Chapter 11

Photonic Crystals and Resonators

In recent years, artificial optical materials and structures enabled the observation of various new optical effects and experiments. For example, photonic crystals are able to inhibit the propagation of certain light frequencies and provide the unique ability to guide light around very tight bends and along narrow channels. On the other hand, the high field strengths in optical microresonators lead to nonlinear optical effects that are important for future integrated optical networks. This chapter explains the basic underlying principles of these novel optical structures. For a more detailed overview the reader is refered to review articles and books listed in the references.

11.1 Photonic Crystals

Photonic crystals are materials with a spatial periodicity in their dielectric constant. Under certain conditions, photonic crystals can create a photonic bandgap, i.e. a frequency window in which propagation through the crystal is inhibited. Light propagation in a photonic crystal is similar to the propagation of electrons and holes in a semiconductor. An electron passing through a semiconductor experiences a periodic potential due to the ordered atomic lattice. The interaction between electron and the periodic potential results in the formation of energy bandgaps. It is not possible for the electron to pass through the crystal if its energy falls in the range of the bandgap. However, defects or a break in the periodicity of the lattice can locally distroy the bandgap and give rise to interesting electronic properties. If the electron is replaced by a photon and the atomic lattice by a material with a periodic dielectric constant we end up with basically the same effects. However, while atoms arrange naturally

to form a periodic structure, photonic crystals need to be fabricated artificially. One exception are gemstone opals which are formed by a spontaneous organization of colloidal silica spheres into a crystalline lattice. In order for a particle to interact with its periodic environment, its wavelength must be comparable to the periodicity of the lattice. Therefore, for photonic crystals the lattice constant must be in the range of $100nm - 1\mu m$. This size range can be accessed with conventional nanofabrication and self-assembly techniques.

To calculate the optical modes in a photonic crystal one needs to solve Maxwell's equations in a periodic dielectric medium. Although this task is much simpler than the calculation of electron propagation in semiconductors where many-particle interactions have to be taken into account, it is not possible to analytically solve Maxwell's equations for two- or three-dimensional periodic lattices. Instead, computational techniques have to be involved. However, many interesting phenomena can be deduced from the simpler one-dimensional case, the periodically layered medium. The developed understanding and intuition will help us to discuss the properties of the more complex two- and three dimensional photonic crystals. A more detailed account on photonic crystals can be found in Refs. [1, 2].

11.1.1 The photonic bandgap

Let us consider a material made of an infinite number of planar layers of thickness d oriented perpendicular to the direction z as shown in Fig. 11.2. The dielectric constant of the layers is alternating between the values ε_1 and ε_2 and the optical mode propagating inside the material is characterized by the wavevector $\mathbf{k} = (k_x, k_y, k_z)$. It is assumed that both materials are non-magnetic, i.e. $\mu_1 = \mu_2 = 1$, and loss-less. We

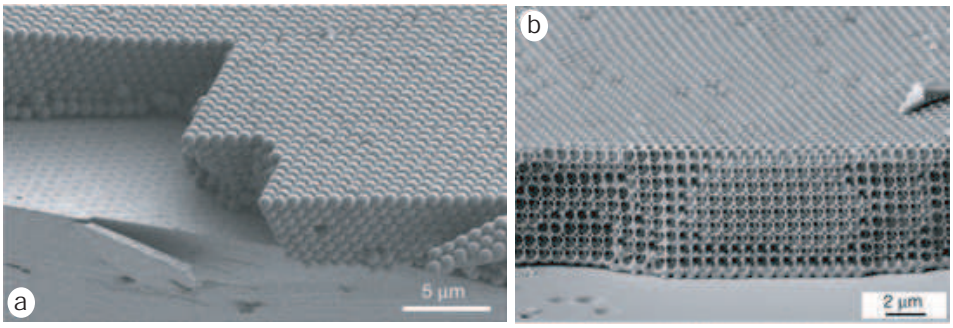

Figure 11.1: Fabrication of silicon photonic bandgap crystals. (a) Template produced by 855nm silica spheres deposited on a Si waver. (b) Photonic crystal obtained after filling the interstitial spaces with high-index Si and removing the template by wet etching. From [3].

can distinguish two kinds of modes, TE modes for which the electric field vector is always parallel to the boundaries between adjacent layers and TM modes for which the magnetic field vector is always parallel to the boundaries. Separation of variables leads to the following ansatz for the complex field amplitudes

$$\text{TE}: \quad \mathbf{E}(\mathbf{r}) = E(z)\,\mathrm{e}^{i(k_x x + k_y y)}\,\mathbf{n}_x\,, \tag{11.1}$$

$$\text{TM}: \quad \mathbf{H}(\mathbf{r}) = H(z)\,\mathrm{e}^{ik_x x + k_y y)}\,\mathbf{n}_x\,. \tag{11.2}$$

In each layer n, the solution for $E(z)$ and $H(z)$ is a superposition of a forward and a backward propagating wave, i.e.

$$\text{TE}: \quad E_{n,j}(z) = a_{n,j}\,\mathrm{e}^{ik_{z_j}(z-nd)} + b_{n,j}\,\mathrm{e}^{-ik_{z_j}(z-nd)}\,, \tag{11.3}$$

$$\text{TM}: \quad H_{n,j}(z) = a_{n,j}\,\mathrm{e}^{ik_{z_j}(z-nd)} + b_{n,j}\,\mathrm{e}^{-ik_{z_j}(z-nd)}\,, \tag{11.4}$$

where $a_{n,j}$ and $b_{n,j}$, are constants which depend on the layer number n and the medium ε_j. The longitudinal wavenumber k_{z_j} is defined as

$$k_{z_j} = \sqrt{\frac{\omega^2}{c^2}\,\varepsilon_j - k_\parallel^2}\,, \quad k_\parallel = \sqrt{k_x^2 + k_y^2}\,, \tag{11.5}$$

with $k_\parallel$ being the parallel wavenumber. To find the constants $a_{n,j}$, $b_{n,j}$ we apply the boundary conditions at the interface $z = z_n = nd$ between the $n-th$ and the $(n+1)-th$ layer

$$\text{TE}: \quad E_{n,1}(z_n) = E_{n+1,2}(z_n)\,, \tag{11.6}$$

$$\frac{d}{dz}E_{n,1}(z_n) = \frac{d}{dz}E_{n+1,2}(z_n)\,, \tag{11.7}$$

$$\text{TM}: \quad H_{n,1}(z_n) = H_{n+1,2}(z_n)\,, \tag{11.8}$$

$$\frac{1}{\varepsilon_1}\frac{d}{dz}H_{n,1}(z_n) = \frac{1}{\varepsilon_2}\frac{d}{dz}H_{n+1,2}(z_n)\,. \tag{11.9}$$

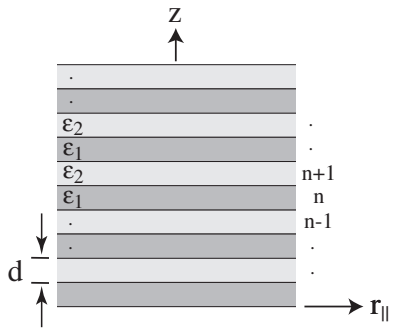

Figure 11.2: One-dimensional photonic crystal made of an infinite number of planar layers of thickness d.

The second equation is arrived at by expressing the transverse component of the magnetic field in terms of the electric field by using $\nabla \times \mathbf{E} = i\omega\mu_o\mathbf{H}$. Similarly, the fourth equation follows from $\nabla \times \mathbf{H} = -i\omega\varepsilon_o\varepsilon\mathbf{E}$. Inserting Eqs. (11.3) and (11.4) leads to

$$a_{n,1} + b_{n,1} = a_{n+1,2}\, \mathrm{e}^{-ik_{z_2}\, d} + b_{n+1,2}\, \mathrm{e}^{ik_{z_2}\, d}\,, \tag{11.10}$$

$$a_{n,1} - b_{n,1} = p_m \left[a_{n+1,2}\, \mathrm{e}^{-ik_{z_2}\, d} - b_{n+1,2}\, \mathrm{e}^{ik_{z_2}\, d}\right]\,, \tag{11.11}$$

where $p_m \in \{p_{TE}, p_{TM}\}$ is a factor which depends on the polarization as

$$p_{TE} = \frac{k_{z_2}}{k_{z_1}} \quad \text{(TE modes)}, \qquad p_{TM} = \frac{k_{z_2}}{k_{z_1}}\frac{\varepsilon_1}{\varepsilon_2} \quad \text{(TM modes)}\,. \tag{11.12}$$

For a given mode type we have two equations but four unknowns, i.e. $a_{n,1}$, $b_{n,1}$, $a_{n+1,2}$, and $b_{n+1,2}$. Thus, we need more equations. Evaluating the boundary conditions at the interface $z = z_{n-1} = (n-1)d$ between the $(n-1)-th$ and the $n-th$ layer leads to

$$a_{n-1,2} + b_{n-1,2} = a_{n,1}\, \mathrm{e}^{-ik_{z_1}\, d} + b_{n,1}\, \mathrm{e}^{ik_{z_1}\, d}\,, \tag{11.13}$$

$$a_{n-1,2} - b_{n-1,2} = \frac{1}{p_m}\left[a_{n,1}\, \mathrm{e}^{-ik_{z_1}\, d} - b_{n,1}\, \mathrm{e}^{ik_{z_1}\, d}\right]\,. \tag{11.14}$$

Although we now have four equations for each mode type, we also increased the number of unknowns by two, i.e. by $a_{n-1,2}$ and $b_{n-1,2}$. However, $a_{n-1,2}$ and $b_{n-1,2}$ can be expressed in terms of $a_{n+1,2}$ and $b_{n+1,2}$ with the help of the *Floquet-Bloch theorem* [4, 5]. The theorem states that if E is a field in a periodic medium with periodicity $2d$ then it has to satisfy

$$\boxed{E(z+2d) = \mathrm{e}^{ik_B 2d}\, E(z)}\,, \tag{11.15}$$

where k_B is a yet undefined wavevector, called the *Bloch wavevector*. A similar equation holds for the magnetic field $H(z)$. The Floquet-Bloch theorem has to be viewed as an *ansatz*, a trial function for our system of coupled differential equations. Application of the Bloch-Floquet theorem leads to

$$\left[a_{n+1,2} + b_{n+1,2}\, \mathrm{e}^{-2ik_{z_2}[z-(n-1)d]}\right] = \mathrm{e}^{ik_B 2d}\left[a_{n-1,2} + b_{n-1,2}\, \mathrm{e}^{-2ik_{z_2}[z-(n-1)d]}\right]. \tag{11.16}$$

Since this equation has to hold for any position z, we have to require that

$$a_{n+1,2} = a_{n-1,2}\, \mathrm{e}^{ik_B 2d}\,, \tag{11.17}$$

$$b_{n+1,2} = b_{n-1,2}\, \mathrm{e}^{ik_B 2d}\,, \tag{11.18}$$

which reduces the number of unknowns from six to four and allows us to solve the *homogeneous* system of equations defined by Eqs. (11.10)- (11.14). The system of

equations can be written in matrix form and the determinant must be zero in order to guarantee a solution. The resulting *characteristic equation* turns out to be

$$\cos(2k_B d) \;=\; \cos(k_{z_1} d)\cos(k_{z_2} d) \;-\; \frac{1}{2}\left[p_m + \frac{1}{p_m}\right]\sin(k_{z_1} d)\sin(k_{z_2} d)\;. \qquad (11.19)$$

Since $\cos(2k_B d)$ is always in the range of $[-1\,..\,1]$, solutions cannot exist when the absolute value of the right hand side is larger than one. This absence of solutions gives rise to the formation of *band gaps*. For example, a wave at normal incidence ($k_{z_1} = \sqrt{\varepsilon_1}\omega/c$, $k_{z_2} = \sqrt{\varepsilon_2}\omega/c$) to a photonic crystal with $\varepsilon_1 = 2.25$, $\varepsilon_2 = 9$ can propagate for $\lambda = 12\,d$ but not for $\lambda = 9\,d$.

For each Bloch wavevector k_B one finds a dispersion relation $\omega(k_\parallel)$. If all possible dispersion relations are plotted on the same graph one obtains a so-called *band-diagram*. An example is shown in Fig. 11.3 where the shaded areas correspond to allowed bands for which propagation through the crystal is possible. Notice, that propagating modes exist even if one of the longitudinal wavenumbers (k_{z_j}) is imaginary. The Bloch-wavevector at the band-edges is determined by $k_B d = n\pi/2$. For a given direction of propagation characterized by $k_\parallel$ one finds frequency regions for which propagation through the crystal is possible and frequency regions for which

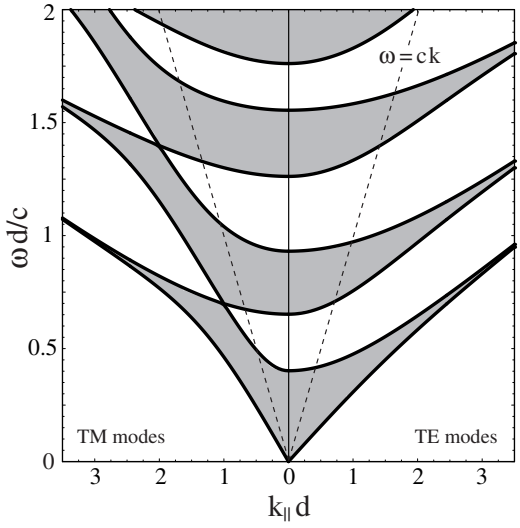

Figure 11.3: Band-diagram for a one-dimensional photonic crystal. The shaded areas are the allowed bands. The diagram represents both TE and TM modes. For a 1D photonic crystal, there are no complete bandgaps, i.e. there are no frequencies for which propagation is inhibited in all direction. Values used: $\varepsilon_1 = 2.33$ (SiO_2), $\varepsilon_2 = 17.88$ ($InSb$).

propagation is inhibited. However, for a one-dimensional crystal there is no *complete bandgap*, i.e. there are no frequencies for which propagation is inhibited in all directions. If a wave propagating in vacuum is directed onto the photonic crystal, then only modes with $k_{\|}$-values smaller than $k = \omega/c$ can be excited. The vacuum light-lines are indicated in the figure and one can find complete frequency bandgaps inside the region $k_{\|} < k$. For these frequencies the photonic crystal is a perfect mirror.

A complete bandgap is possible in $2D$ and $3D$ photonic crystals. It is favorable if the dielectric constants of the media differ by a large amount. The volume ratio between the two media is also important. Unfortunately, the solutions of $2D$ and $3D$ photonic crystals cannot be found by analytical means, but efficient numerical techniques have been developed over the past few years.

In semiconductors, the valence band corresponds to the topmost filled energy band for which electrons are attached to the ion cores. On the other hand, if electrons are excited into the next higher band, the conduction band, they become delocalized and conduction through the crystal strongly increases. The situation is similar for photonic crystals: the band below a bandgap is refered to as the *dielectric band* and the band above the bandgap as the *air band*. In the dielectric band, the optical energy is confined inside the material with the higher dielectric constant, whereas in the air band the energy is found to be in the material with lower dielectric constant. Thus, excitation from one band to another promotes the optical energy from the high dielectric to the low dielectric material.

A photonic crystal can also strongly affect the spontaneous emission rate of an embedded quantum system such as an atom or a molecule. For example, the excited state of an atom cannot couple to any radiation modes if the transition frequency between excited state and ground state lies in the bandgap region of the photonic crystal. In this case, spontaneous emission is severely inhibited and the atom will reside in its excited state. As discussed later, a localized defect near the atom can have the opposite effect and enhance the emission rate of the atom significantly.

11.1.2 Defects in photonic crystals

Defects in photonic crystals are introduced to localize or guide light. While photons with energies within the photonic bandgap cannot propagate through the crystal, they can be confined to defect regions. A line of defects opens up a waveguide: light with a frequency within the bandgap can only propagate along the channel of defects since it is repelled from the bulk crystal. Waveguides in photonic crystals can transport light around tight corners with almost no loss. Furthermore, photonic crystal waveguides can be composed of air channels thereby significantly reducing group

velocity dispersion. A short pulse of light can travel large distances without being temporally broadened. Photonic crystal waveguides are of great practical importance for miniaturized optoelectronic circuits and devices. As an example, Fig. 11.4 shows a waveguide T-junction in a photonic crystal. The line-defects are created by dislocating certain portions of the crystal and by removing a row of elements [6]. The device functions as a diplexer, i.e. high frequencies are deflected to the left and low frequencies are deflected to the right. To improve the performance, an additional perturbation has been added to the intersection region.

While defect arrays in photonic crystals are introduced primarily for waveguide applications, localized defects are intended to trap light. Optical cavities formed by localized defects can have very high quality factors, a prerequisite for various nonlinear optical effects and laser applications. Fig. 11.5 shows a 2D photonic crystal with a single central defect [7]. A laser is formed by embedding the photonic crystal in between two Bragg mirrors acting as the end mirrors of a laser cavity. The lateral confinement is provided by the photonic crystal.

Photonic crystal cavities can also be used to control the spontaneous emission rate of quantum systems located in the defect region. Depending on the physical properties of the cavity, the local density of states (DOS) at the emission wavelength λ_o of the quantum system can be increased or decreased over the free space DOS (see section **??**). The local DOS at λ_o depends on the ability of the cavity to store energy at the emission wavelength λ_o. Thus, the higher the quality factor $Q = \omega_o/\Delta\omega$ is, the higher the DOS will be. The density of states in a large cavity can be approximated

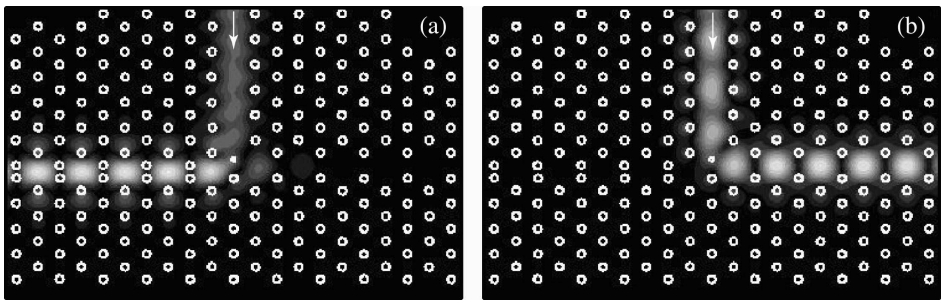

Figure 11.4: 2D photonic crystal diplexer. A waveguide T-junction is formed by dislocations and removal of elements. High frequencies are deflected to the left and low frequencies are deflected to the right. The figure shows the computed optical intensity for (a) $\omega = 0.956\pi c/d$ and (b) $\omega = 0.874\pi c/d$, with d being the lattice constant. From [6].

as

$$\rho \;=\; \frac{1}{\omega_o}\frac{D\,Q}{V}\;, \tag{11.20}$$

where V is the volume of the cavity and D is the mode degeneracy, i.e. the number of cavity modes with the same frequency. On the other hand, the free space DOS has been derived in Eq. (**??**) as

$$\rho_o \;=\; \frac{1}{\omega_o}\frac{8\pi}{\lambda_o^3}\;. \tag{11.21}$$

Thus, the spontaneous decay rate is enhanced by a factor of

$$K \;=\; \frac{\rho}{\rho_o} \;=\; \frac{D}{8\pi}\,Q\,\frac{\lambda_o^3}{V} \tag{11.22}$$

near a photonic crystal cavity. Strong enhancement depends on a small cavity volume and a high Q-factor.

11.2 Optical Microcavities

Optical microcavities formed by dielectric spheres attracted considerable interest in various fields of research. The high quality factors associated with the resonant modes have inspired experiments in cavity quantum electrodynamics, gave rise to sensitive biosensors, and the high energy density in the cavities allowed researchers to observe various nonlinear processes such as switching of coherent light, low-threshold lasing, or stimulated Raman scattering [9].

To understand these processes it is necessary to solve Maxwell's equations for the simple geometry of a sphere. The mathematical basis is identical with the famous Mie

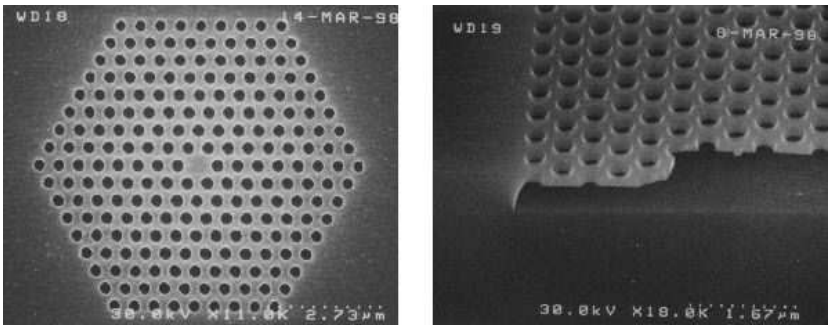

Figure 11.5: Top view and cross-section of a 2D photonic crystal with a single central defect. The crystal consists of a microfabricated hexagonal array of air holes in $InGaAsP$ and the defect is introduced by a filled central hole. From [7].

theory and the details are found in various excellent books such as Ref. [8]. Although the Mie theory is in excellent agreement with experimental measurements, the convergence of the expansions is very slow for spheres with diameters $D \gg \lambda$ [10]. For such spheres it is observed that small variations in the initial conditions (size, dielectric constant) lead to considerable variations of the scattering cross-section. These variations, called ripples, can be associated with sphere resonances. For each ripple peak, light remains trapped for a long time inside the sphere and orbits near the surface by multiple total internal reflections. These resonant modes are called *whispering gallery modes* or *morphology dependent resonances*. The Q-factors of the resonant modes are always finite but they can be theoretically as large as 10^{21}. Consequently, the resonant modes are leaky modes and the sphere is a non-conservative system because energy is permanently lost due to radiation. The largest experimentally observed Q-factors are on the order of $Q = 10^{10}$.

Instead of reproducing the full Mie theory, we intend to provide an intuitive picture for the resonances occuring in optical microspheres. The picture has been developed by Nussenzveig and Johnson [10, 11] and is called the *effective potential approach*. It has a direct analogy to the quantum mechanical theory of a finite spherical well. The finite Q-factors of microspheres can be associated with the phenomenon of tunneling.

Let us consider a homogeneous sphere with dielectric constant ε_1 and radius a surrounded by a homogeneous medium with dielectric constant ε_2. The complex field amplitudes inside and outside of the sphere have to satisfy the vector Helmholtz equation

$$\left[\nabla^2 + \frac{\omega^2}{c^2}\,\varepsilon_i\right]\mathbf{E}(\mathbf{r}) = \mathbf{0}\,, \tag{11.23}$$

where $i \in [1, 2]$, depending on whether the field is evaluated inside or outside of the sphere. A similar equation can be written down for the magnetic field $\mathbf{H}$. Using the mathematical identity

$$\nabla^2\left[\mathbf{r}\cdot\mathbf{E}(\mathbf{r})\right] = \mathbf{r}\cdot\left[\nabla^2\mathbf{E}(\mathbf{r})\right] + 2\nabla\cdot\mathbf{E}(\mathbf{r})\,, \tag{11.24}$$

setting the last term equal to zero, and inserting into Eq. (11.23), leads to the scalar Helmholtz equation

$$\left[\nabla^2 + \frac{\omega^2}{c^2}\,\varepsilon_i\right] f(\mathbf{r}) = 0\,, \qquad f(\mathbf{r}) = \mathbf{r}\cdot\mathbf{E}(\mathbf{r})\,. \tag{11.25}$$

Separation of variables yields

$$f(r, \vartheta, \varphi) = Y_l^m(\vartheta, \varphi)\, R_l(r), \tag{11.26}$$

with Y_l^m being the spherical harmonics and R_l being a solution of the radial equation

$$\left[\frac{d}{dr^2} + \left(\frac{\omega^2}{c^2}\,\varepsilon_i - \frac{l(l+1)}{r^2}\right)\right] rR_l(r) = 0\,. \tag{11.27}$$

Solutions of this equation are the spherical Bessel functions (c.f. Section **??**).

A similar equation is encountered in quantum mechanics. For a spherically symmetric potential $V(\mathbf{r})=V(r)$ one obtains the radial Schrödinger equation

$$\left[-\frac{\hbar^2}{2m}\frac{d}{dr^2} \; + \; \left(V(r) \; + \; \frac{\hbar^2}{2m}\frac{l(l+1)}{r^2}\right)\right] \, rR_l(r) \; = \; E\, rR_l(r) \; , \tag{11.28}$$

where $\hbar$ is the reduced Planck's constant and m the effective mass. Besides the centrifugal term with $1/r^2$ dependence, the equation is identical in form to the one-dimensional Schrödinger equation. The expression in the round brackets is called the *effective potential* $V_{eff}(r)$.

The similarity between the electromagnetic and the quantum mechanical problem allows us to introduce an effective potential V_{eff} and an energy E for the dielectric sphere. From the identity of the two equations in free-space ($V=0$, $\varepsilon_i=1$) we find

$$E \; = \; \frac{\hbar^2}{2m}\frac{\omega^2}{c^2} \; . \tag{11.29}$$

With this definition, the effective potential of the dielectric sphere turns out to be

$$\boxed{V_{eff}(r) = \frac{\hbar^2}{2m}\left[\frac{\omega^2}{c^2}(1-\varepsilon_i) \; + \; \frac{l(l+1)}{r^2}\right]} \; . \tag{11.30}$$

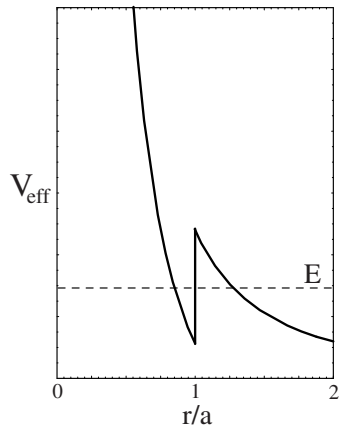

Figure 11.6: Effective potential V_{eff} for a dielectric sphere according to Eq. (11.30). The radiative decay of a resonant mode can be associated with energy tunneling through the potential barrier. The following parameters were used: $\varepsilon_1=2.31$, $\varepsilon_2=1$, $\lambda=800nm$, $l=500$, and $a=50\mu m$.

Fig. 11.6 shows the effective potential for a dielectric sphere in air. The abrupt change of ε at the boundary of the sphere gives rise to a discontinuity in V_{eff} and thus to a potential well. The horizontal line in the figure indicates the energy E as defined in Eq. (11.29). Notice, that unlike in quantum mechanics the energy E depends on the shape of the potential well. Thus, a change of V_{eff} will also affect E.

Similar to quantum mechanical tunneling, the finite height of the potential barrier gives rise to energy leakage through the barrier. Thus, a resonant mode in the optical microcavity will damp out with a characteristic time defined by the tunneling rate through the barrier. In quantum mechanics, only discrete energy values are possible for the states within the potential well. These values follow from an energy eigenvalue equation defined by the boundary conditions. The situtaion is similar for the electromagnetic problem where we can distinguish between to kinds of modes, TE modes and TM modes. They are defined as

$$TE \text{ modes}: \quad \mathbf{r} \cdot \mathbf{E}(\mathbf{r}) = 0 \tag{11.31}$$

$$TM \text{ modes}: \quad \mathbf{r} \cdot \mathbf{H}(\mathbf{r}) = 0\ . \tag{11.32}$$

For TE modes, the electric field is always transverse to the radial vector and for TM modes the same holds for the magnetic field.

The boundary conditions at the surface of the sphere ($r = a$) connect the interior fields with the exterior fields. The radial dependence of the interior field is expressed in terms of spherical Bessel functions j_l and the exterior field in terms of spherical Hankel functions of the second kind $h_l^{(2)}$. j_l ensures that the field is regular within the sphere whereas $h_l^{(2)}$ is required to fulfill the radiation condition at infinity. The boundary conditions lead to a homogeneous system of equations from which the fol-

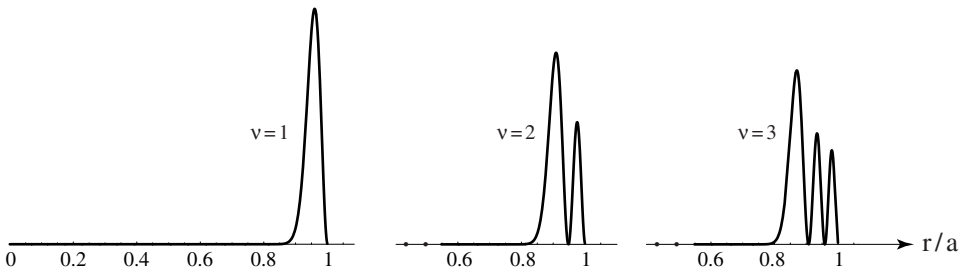

Figure 11.7: Radial energy distribution of TM modes with angular momentum mode number $l = 120$. The microsphere has a dielectric constant of $\varepsilon = 2.31$. The radial mode number ν indicates the number of energy maxima in radial direction.

lowing *characteristic equations* are derived

$$TE \text{ modes}: \quad \frac{\psi_l'(\tilde{n}x)}{\psi_l(\tilde{n}x)} - \tilde{n}\frac{\zeta_l'(x)}{\zeta_l(x)} = 0 \tag{11.33}$$

$$TM \text{ modes}: \quad \frac{\psi_l'(\tilde{n}x)}{\psi_l(\tilde{n}x)} - \frac{1}{\tilde{n}}\frac{\zeta_l'(x)}{\zeta_l(x)} = 0\,. \tag{11.34}$$

Here, the ratio of interior to exterior refractive indices is denoted by $\tilde{n} = \sqrt{\varepsilon_1/\varepsilon_2}$ and x is the size parameter defined as $x = 2\pi k$, with k being the vacuum wavenumber $k{=}\omega/c{=}2\pi/\lambda$. The primes denote differentiations with respect to the argument and ψ_l, ζ_l are Ricatti-Bessel functions defined as

$$\psi_l(z) = z\, j_l(z)\,, \qquad \zeta_l(z) = z\, h_l^{(2)}(z)\,. \tag{11.35}$$

For a given angular momentum mode number l, there are many solutions of the characteristic equations. These solutions are labelled with a new index ν, called the radial mode order. As shown in Fig. 11.7, ν indicates the number of peaks in the radial intensity distribution inside the sphere. From all the possible solutions only those solutions whose energies according to Eq. (11.29) lie in the range of the bottom and top of the potential well are considered resonant modes. Notice that the characteristic equations (11.33) and (11.34) cannot be fulfilled for real x, which means that the eigenfrequencies $\omega_{\nu l}$ are *complex*. Consequently, the modes of the microsphere are *leaky modes* and the stored energy is continuously dissipated through radiation. The real part of $\omega_{\nu l}$ denotes the center frequency ω_o of the mode and the imaginary part indicates half the width $\Delta\omega$ of the resonance. Thus, the Q-factor can be expressed as

$$Q = \frac{\omega_o}{\Delta\omega} = \frac{\mathrm{Re}\{\omega_{\nu l}\}}{2\,|\mathrm{Im}\{\omega_{\nu l}\}|}\,. \tag{11.36}$$

Because of the dissipative nature of the resonances, the modes are referred to as quasi-normal modes.

To better visualize the classification of modes we consider the example of a glass sphere ($a = 10\mu m$, $\varepsilon_1 = 2.31$) in air ($\varepsilon_2 = 1$) and we assume an angular momentum mode number of $l{=}120$. The wavelength of the mode with the highest Q-factor can be estimated by the geometrical requirement that the circumference of the sphere must be a multiple of the internal wavelength

$$\text{highest}-\text{Q mode}: \; l \approx nka\,, \tag{11.37}$$

where n is the interior index of refraction. For the present example we find $\lambda \approx 796nm$ or $x \approx 79$ and the spectral separation between adjacent l-modes is $\Delta\lambda \approx \lambda^2/(2\pi an) = 6.6nm$.

Solving Eq. (11.33) for $l = 120$ yields the values (real parts) $\lambda^{TE}_{1,120} = 743.25\,nm$, $\lambda^{TE}_{2,120} = 703.60\,nm$, $\lambda^{TE}_{3,120} = 673.35\,nm$, .. . Similarly, the solutions of Eq. (11.34) are $\lambda^{TM}_{1,120} = 739.01\,nm$, $\lambda^{TM}_{2,120} = 699.89\,nm$, $\lambda^{TM}_{3,120} = 670.04\,nm$, .. . The $\nu = 1$ modes, with a single energy maximum inside the sphere, have the highest Q-factors. Their wavelengths are in rough agreement with the estimate of $\lambda \approx 796nm$ according to Eq. (11.37). TM modes exhibit shorter wavelengths than TE modes. Generally, the Q-factor decreases with increasing radial mode number. For the current example, the Q-factor decreases from $\approx 10^{17}$ for the $\nu = 1$ modes to $\approx 10^6$ for the $\nu = 6$ modes. Fig. 11.8 shows the spectral positions of the $l = 119$, $l = 120$, and $l = 121$ modes. The spacing between same l-modes is $\approx 6\,nm$, in agreement with the previous estimate. Modes are represented as vertical lines, the height of which indicates the Q-factor on a logarithmic scale. Solid lines are TE modes and dashed lines are TM modes. A dense network of modes is formed when all l-modes are plotted on the same axis. Furthermore, since the azimuthal modes (mode number m) are degenerate each l-mode consists of a multitude of submodes. The degeneracy is lifted by geometrical asymmetries or material imperfections resulting in even more mode frequencies.

The calculated Q-factors account only for radiation losses. For microspheres with $a > 500\mu m$ theses Q-factors can be larger than 10^{20}. However, the highest measured Q-factors are on the order of 10^{10} indicating that other contributions such as surface roughness, shape deformations, absorption, or surface contamination are the limiting factors for a high Q. These factors can be taken into account by defining the total

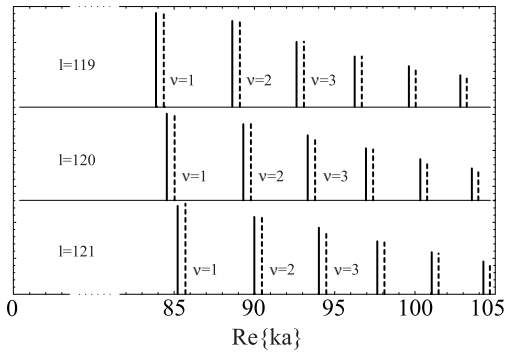

Figure 11.8: Normalized mode frequencies for a microsphere with $\varepsilon = 2.31$ and angular momentum mode numbers $l = 119$, $l = 120$, and $l = 121$. Solid lines are TE modes and dashed lines are TM modes. The height of the lines indicates the quality factor on a logarithmic scale. The $\nu = 1$ modes have a Q-factor of $\approx 10^{17}$ and the $\nu = 6$ modes $\approx 10^6$.

quality factor of a particular microcavity mode as

$$\frac{1}{Q_{tot}} \;=\; \frac{1}{Q} \,+\, \frac{1}{Q_{other}}\,, \tag{11.38}$$

where Q is the radiation limited, theoretical quality factor and Q_{other} accounts for all other contributions. Usually, Q can be neglected in comparison to Q_{other}. Near a resonance with angular frequency ω_o, the electric field takes on the form

$$\mathbf{E}(t) \;=\; \mathbf{E}_o \,\exp\left[(i\omega_o \,-\, \frac{\omega_o}{2\,Q_{tot}})\,t\right]\,, \tag{11.39}$$

and the stored energy density assumes a Lorentzian distribution

$$W_\omega(\omega) \;=\; \frac{\omega_o^2}{4Q_{tot}^2}\,\frac{W_\omega(\omega_o)}{(\omega-\omega_o)^2 \,+\, (\omega_o\,/\,2Q_{tot})^2}\,. \tag{11.40}$$

The mode structure of a microsphere gives rise to a discrete photonic density of states ρ as qualitatively illustrated in Fig. 11.9. ρ depends on the position relative to the microsphere and on the orientation of the transition dipole (c.f. Section **??**). Efficient energy transfer between molecules and other quantum systems can only be accomplished within the narrow frequency windows of individual resonant modes. Also, the excited state lifetime of a molecule is strongly reduced if its emission frequency coincides with the frequency of a resonant mode. On the other hand, the lifetime can be drastically prolonged if the emission frequency is between two mode frequencies. If the emission bandwidth of a molecule spans over several mode frequencies, the fluorescence spectrum will consist of discrete lines. The same is true for the absorption spectrum. Thus, the free space spectra of emission and absorption are sampled with the discrete mode spectrum of a microcavity. Since energy transfer between molecules depends on the overlap of emission and absorption spectra (c.f.

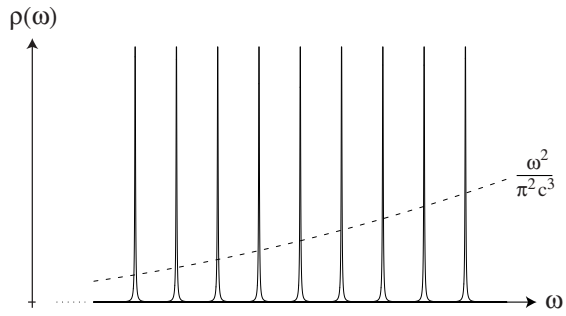

Figure 11.9: Photonic density of states of a microsphere (solid line) and in free space (dashed line). In a microsphere all energy is concentrated in the narrow frequency windows of individual resonant modes.

Section **??**) it is expected, at first glance, that the energy transfer efficiency is reduced in or near a microcavity because the overlap-bandwidth associated with the narrow mode frequencies is drastically reduced compared with the free space situation. However, for a high-Q cavity this is not the case because the density of states at the frequency of a resonant mode is so high that the overlap integral becomes much larger than in free space, despite of the narrower bandwidth. Arnold and coworkers have shown that energy transfer in a microsphere can be several orders more efficient than in free space [9] making microspheres promising candidates for long-range energy transfer. Microspheres were used in applications such as biosensors, optical switching, and cavity QED. Various other experiments can be thought of such as two-photon energy-transfer, and exciting results can be expected in the near future.

Problems

Problem 11.1 Consider a one-dimensional photonic crystal made of two alternating dielectric layers with the dielectric constants ε_1 and ε_2 and *different* thicknesses d_1 and d_2. Derive the characteristic equation for TE and TM modes. Plot the dispersion curves $k_x(\omega)$ for $\varepsilon_1 = 17.88$, $\varepsilon_2 = 2.31$, and $d_2/d_1 = 2/3$.

Problem 11.2 Estimate the wavelength of the highest-Q mode of a microsphere with radius $a = 50\mu m$ and dielectric constant $\varepsilon = 2.31$. Determine the spacing $\Delta\lambda$ between modes.

Problem 11.3 For a microsphere with $\varepsilon = 2.31$, plot numerically the right hand sides of Eq. (11.33) and Eq. (11.34) in the complex ka plane. Assume an angular momentum mode number $l = 10$ and estimate the value ka for modes with radial mode numbers $\nu = 1, 2, 3$.

References

[1] J. D. Joannopoulos, R. D. Meade, J. N. Winn, *Photonic Crystals*, Princeton Univ Press (1995).

[2] J. D. Joannopoulos, P. R. Villeneuve, and S. Fan, "Photonic crystals: putting a new twist on light," *Nature* **386**,143–149 (1997).

[3] Y. A. Vlasov, X. Z. Bo, J. C. Sturm, and D. J. Norris, "On-chip natural assembly of silicon photonic bandgap crystals," *Nature* **414**, 289–293 (2001).

[4] G. Floquet, "Sur les équations differentielles linéaries à coeffcients périodiques," *Ann. Ecole Norm. Sup.* **12**, 47–88 (1883).

[5] F. Bloch, "Über die Quantenmechanik der Elektronen in Kristallgittern," *Z. Phys.* **52**, 555–600 (1929).

[6] E. Moreno, D. Erni, and Ch. Hafner, "Modeling of discontinuities in photonic crystal waveguides with the multiple multipole method," *Phys. Rev. E* **66**, 036618 (2002).

[7] O. J. Painter, A. Husain, A. Scherer, J. D. O'Brien, I. Kim, and P. D. Dapkus, "Two-dimensional photonic crystal defect laser," *J. Lightwave Techn.* **17**, 2082-2089 (1999).

[8] C. G. Bohren and D. R. Huffman, *Absorption and Scattering of Light by Small Particles*, John Wiley, New York (1983).

[9] R. K. Chang and A. J. Campillo (eds.), *Optical Processes in Microcavities*, Advanced Series in Applied Physics **3**, World Scientific, Singapore (1996).

[10] H. M. Nussenzveig, *Diffraction Effects in Semiclassical Scattering.* Cambridge University Press, Cambridge (1992).

[11] B. R. Johnson, "Theory of morphology-dependent resonances: shape resonances and width formulas," *J. Opt. Soc. A* **10**, 343–352 (1993).